

UEPS: Robust and Efficient MRI Reconstruction

Xiang Zhou^{1,2*}, Hong Shang^{1*}, Zijian Zhan^{1,2}, Tianyu He^{1,3}, Jintao Meng^{1,4†},
and Dong Liang^{1,5†}

¹ Shenzhen Institutes of Advanced Technology, Chinese Academy of Sciences, China

² School of Biomedical Engineering, Shenzhen University Medical School, Shenzhen University, China

³ University of Chinese Academy of Sciences, China

⁴ Faculty of Computer Science and Artificial Intelligence, Shenzhen University of Advanced Technology, China

⁵ State Key Laboratory of Biomedical Imaging Science and System, Chinese Academy of Sciences, China

Abstract. Deep unrolled models (DUMs) have become the state of the art for accelerated MRI reconstruction, yet their robustness under domain shift remains a critical barrier to clinical adoption. In this work, we identify coil sensitivity map (CSM) estimation as the primary bottleneck limiting generalization. To address this, we propose UEPS, a novel DUM architecture featuring three key innovations: (i) an Unrolled Expanded (UE) design that eliminates CSM dependency by reconstructing each coil independently; (ii) progressive resolution, which leverages k-space-to-image mapping for efficient coarse-to-fine refinement; and (iii) sparse attention tailored to MRI’s 1D undersampling nature. These physics-grounded designs enable simultaneous gains in robustness and computational efficiency. We construct a large-scale zero-shot transfer benchmark comprising 10 out-of-distribution test sets spanning diverse clinical shifts—*anatomy, view, contrast, vendor, field strength, and coil configurations*. Extensive experiments demonstrate that UEPS consistently and substantially outperforms existing DUM, end-to-end, diffusion, and untrained methods across all OOD tests, achieving state-of-the-art robustness with low-latency inference suitable for real-time deployment. Our code is available at <https://github.com/HongShangGroup/UEPS>.

Keywords: Accelerated MRI · Deep unrolled models · Sparse attention

1 Introduction

Magnetic resonance imaging (MRI) is indispensable in modern medicine due to its unique soft-tissue contrast and radiation-free nature, but suffers from intolerable long scan time. Undersampled MRI is an active research field for solving the ill-posed inverse problem of reconstructing high-fidelity images from only a fraction of the measurements in k-space to accelerate MRI scan. Current state-of-the-art methods for undersampled MRI are predominantly based on deep

*Equal contribution.

†Corresponding authors: {jt.meng, dong.liang}@siat.ac.cn

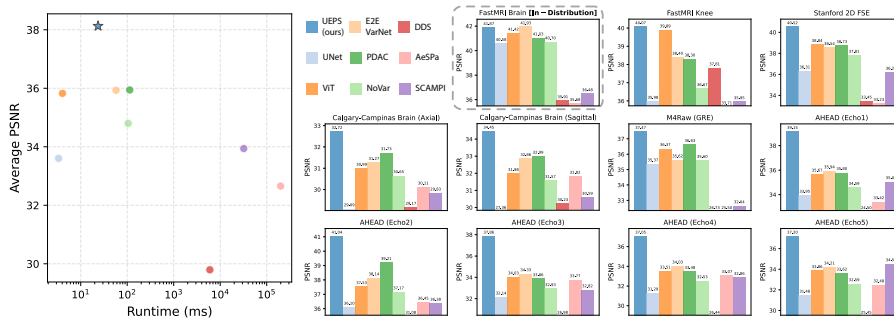


Fig. 1: Zero-shot transfer benchmark results. Average PSNR: mean over 10 OOD sets. Runtime: measured on FastMRI Knee (15 coils).

unrolled models (DUM) which integrate a physical forward model of the imaging process into learnable neural network and typically trained on large-scale datasets comprising multi-coil k-space measurements [14, 17, 20, 44, 50, 54].

Despite their success on benchmarks with abundant training data [58], DUM struggle with domain shift and transfer poorly to unseen acquisition protocols [7, 21, 25]. To enhance robustness, recent studies have explored training DUM on combined datasets aggregated from multiple sources [29, 30]. Such methods are limited in that the virtually unlimited contrast variability afforded by flexible MRI acquisition makes it infeasible to curate a comprehensive large-scale training dataset. Additionally, the multi-coil raw data for MRI reconstruction are more resource-intensive to collect compared to DICOM images. An alternative class of approaches, known as untrained methods, addresses the robustness problem by eliminating the need for any training data, instead optimizing independently for each test case [8, 16, 22, 26, 31, 42, 55]. These methods avoid learning spurious correlations tied to any specific distribution, however, the severely limited input fundamentally caps the achievable performance universally [7]. Thus, the lack of robustness remains an unresolved barrier impeding the translation of deep learning-based MRI reconstruction into clinical practice.

To address this robustness issue, we first identify the primary generalization bottleneck stems from the dependency of DUM on coil sensitivity maps (CSM). In multi-coil MRI, now the clinical standard, multiple receiver coils simultaneously acquire data, each with a characteristic CSM describing its spatial reception profile. CSM are used in DUM to convert individual coil images into a single image or vice versa. Our analysis uncovers that errors in CSM estimation, which inevitably worsen under domain shift, are amplified as propagating through the rest network, resulting in reconstruction failures. We propose a simple yet effective redesign of DUM, termed Unrolled Expanded model (UE), which reconstructs each individual coil image separately, thereby eliminating the need for CSM and the associated error propagation problem. However, the improved robustness comes with increased computational cost, as runtime scales with the number of coils. We further introduce two key features, progressive resolution and sparse attention, to offset the increased computational burden.

Multi-resolution is a widely adopted concept in vision models as it jointly optimizes speed and performance. Unlike typical image-to-image tasks like image restoration [27, 57, 60], MRI reconstruction is a k-space-to-image mapping, suggesting that the standard down-sampling up-sampling architecture may be suboptimal here. We propose Unrolled Expanded model with Progressive resolution (UEP), whose core innovation lies in performing up-sampling by k-space expansion. Crucially, additional measurements are incorporated for the expanded k-space region, adding authentic high-frequency information, which cannot be achieved by image-space interpolation. As an up-sampling only architecture, early stages run at lower resolution with substantially reduced computation. An additional benefit is the implicit curriculum learning: initial stages with denser k-space sampling pose an easier task, stabilizing training and providing improved initialization for subsequent high-resolution refinement.

Sparse attention serves as another key feature for accelerating our transformer-based model. Recognizing that MRI undersampling, therefore aliasing artifacts, occurs only along a single axis, our sparse attention allocates more computation to this axis, achieving computational savings where full attention is unnecessary. We refer to the proposed Unrolled Expanded model augmented with Progressive resolution and Sparse attention as UEPS.

In this work, we tackle the robustness challenge in deep unrolled MRI reconstruction through a systematic reinvestigation of the model architecture. Our main contributions can be summarized as follows:

1. After identifying CSM error as the root cause of poor generalization, we propose UE that bypasses this bottleneck entirely and achieves markedly better robustness, albeit at the cost of increased computation.
2. We further introduce progressive resolution and sparse attention, two design features that grounded in the k-space-to-image mapping and 1D acceleration nature of MRI physics, which yield marked computational acceleration without compromising, and in fact improving, reconstruction quality.
3. To rigorously assess generalization, we establish a large-scale zero-shot transfer benchmark and show that UEPS outperforms all competing approaches by a significant margin, while maintaining acceptable runtime.

2 Related Work

2.1 Deep Unrolled Models

DUM represents a class of methods that unroll optimization algorithms into network layers, combining the rigor of physics-based models with the representational power of deep learning [2, 17, 39]. The evolution of DUM methods has seen a shift from using pre-computed CSM from external tools [48, 49] to jointly learning them with the reconstruction network [23, 44], a paradigm that underpins all contemporary state-of-the-art (SOTA) DUM methods. Subsequent research has explored diverse architectural innovations to further improve performance, such as convolutional recurrent network [56], hybrid convolutional-transformer

network [14], memory efficient transformer [9], neural operator-based architecture [20], and leveraging adjacent slices input [54]. Despite architectural advances, these works predominantly reports performance on in-distribution test splits of large datasets like FastMRI [58], the real-world robustness of these models when deployed on out-of-domain data remains an open question.

2.2 Multi-Resolution

Multi-resolution architectures are commonly used in low-level vision tasks such as image restoration and medical image reconstruction, leveraging coarse resolutions for computational efficiency and global context while preserving high-resolution pathways for spatial precision. In image restoration, early seminal works [53, 57] employ an Transformer-based U-Shaped structure with downsampling and upsampling, to capture hierarchical multi-scale representation and maintain computational efficiency, which becomes gold standard for subsequent approaches [19, 60]. In MRI reconstruction, DUM approaches consist of cascaded stages, each containing a denoiser, typically implemented as a multi-resolution architecture, ranging from UNet in early works [44] to transformer-based [9, 52] or hybrid convolution-transformer designs [14, 50] in recent approaches. Note this multi-resolution design is within each cascade, to the best of our knowledge, no prior work has explored multi-resolution across cascades. Learned upsampling operations are used in these multi-scale models, such as transposed convolutions [13] or pixel shuffle [41], which are well-suited for image-to-image tasks by learning to synthesize details. However, they cannot utilize the available high-frequency information present in k-space for MRI reconstruction.

2.3 Sparse Attention

Sparse attention has become essential for scaling vision transformers to high-resolution images, where standard self-attention’s quadratic complexity becomes prohibitive. Various strategies have been proposed to restrict attention to relevant subsets to reduce computational cost while largely preserving representational power. Early breakthroughs focused on fixed sparsity patterns like shifted non-overlapping local windows [32], sliding window [18], factorized attention along axes [11, 51]. Beyond static patterns, dynamic sparse attention offers more flexibility by dynamically predicting the most relevant tokens or regions for each query based on the input content. For instance, DynamicViT progressively prunes redundant visual tokens using a lightweight prediction module [37]. SpargeAttn predict the sparse mask by compressing each block of Q, K to a single token, demonstrating universal application on various tasks [59]. Although sparse attention has been extensively studied for vision and language tasks, it remains largely unexplored in MRI reconstruction.

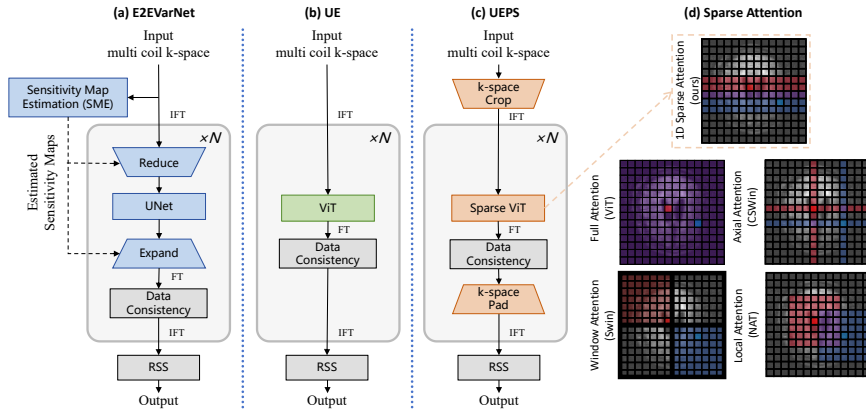


Fig. 2: Overview of the proposed UEPS architecture

3 Proposed Method

UEPS, our proposed architecture, is a deep unrolled model redesigned for robustness without sacrificing efficiency. It consists of three main features, Unrolled Expanded model (UE), progressive resolution, and sparse attention, with entire model shown in Fig. 2. UE primarily improves robustness, but sacrifices speed. Progressive resolution and sparse attention, each motivated by MRI-specific principles, both reduce computation and further improve reconstruction quality.

3.1 Problem Formulation

Modern MRI use multiple receiver coils, each of which measures Fourier components of the imaged volume multiplied by a complex-valued position-dependent CSM [58]. The measured data from i th coil \mathbf{k}_i is given by

$$\mathbf{k}_i = \mathcal{F}(S_i \mathbf{m}) + \epsilon_i, \quad i = 1, 2, \dots, N \quad (1)$$

where \mathbf{m} is the imaging object, S_i is CSM of i th coil, \mathcal{F} is the fourier transform operator, ϵ_i is measurement noise for i th coil, N is the number of coils.

For fully sampled k-space data, i th coil image $\hat{\mathbf{m}}_i$ can be reconstructed simply by an inverse fourier transform

$$\hat{\mathbf{m}}_i = \mathcal{F}^{-1}(\mathbf{k}_i) \quad (2)$$

Then, the individual coil images are combined with pixel-level root-sum-of-squares (RSS) to provide the final image estimate $\hat{\mathbf{m}}$ [58].

$$\hat{\mathbf{m}} = \text{RSS}(\hat{\mathbf{m}}_1, \dots, \hat{\mathbf{m}}_N) = \sqrt{\sum_{i=1}^N |\hat{\mathbf{m}}_i|^2} \quad (3)$$

In undersampled MRI, only part of the k-space is acquired to accelerate scan

$$\tilde{\mathbf{k}}_i = \mathcal{MF}(S_i \mathbf{m}) + \epsilon_i, \quad i = 1, 2, \dots, N \quad (4)$$

where \mathcal{M} is the binary sampling mask, $\tilde{\mathbf{k}}_i$ is undersampled k-space data.

DUM solves this ill-posed inverse problem of reconstructing undersampled MRI by integrating the physical forward model Eq. (1) into a cascaded neural network inspired by iterative optimization algorithms. Let $\mathbf{k}^{(0)} \in \mathbb{C}^{N \times H \times W}$ denote the cartesian k-space data from all coils with unsampled points filled with zeros. H/W is the number of readout samples/phase encoding in k-space, equivalent to height/width in image-space for cartesian MRI. Let $\mathbf{x}^{(t)} \in \mathbb{C}^{N \times H \times W}$ denote the intermediate multi-coil image estimate at the t -th cascade of the unrolled model, and $\mathbf{k}^{(t)} \in \mathbb{C}^{N \times H \times W}$ the corresponding intermediate k-space estimate. Each refinement stage can be formulated as below with image-space intermediate quantities

$$\tilde{\mathbf{x}}^{(t)} = \mathbf{x}^{(t)} + \mathcal{E}(\mathcal{D}_\theta^{(t)}(\mathcal{R}(\mathbf{x}^{(t)}))) \quad (5)$$

$$\mathbf{k}^{(t)} = \mathcal{F}(\tilde{\mathbf{x}}^{(t)}) \quad (6)$$

$$\mathbf{k}^{(t+1)} = \mathcal{DC}_\eta(\mathbf{k}^{(t)}, \mathbf{k}^{(0)}) \quad (7)$$

$$\mathbf{x}^{(t+1)} = \mathcal{F}^{-1}(\mathbf{k}^{(t+1)}) \quad (8)$$

where \mathcal{R} and \mathcal{E} are reduction and expansion operator to convert multi-coil images into a single image or vice versa by leveraging CSM with details refers to [44]. $\mathcal{D}_\theta^{(t)}$ is a learnable image denoiser, such as UNet [44], Restormer [9], or ViT [12, 28, 35] used in this work. \mathcal{DC}_η is the data consistency module with learnable weight η . While originally inspired by the gradient descent formulation of compressed sensing MRI, this module can accommodate various implementations, provided that data fidelity with acquired measurements is maintained. Notably, with the specific instantiation below with scalar η , Eqs. (5) to (8) is mathematically equivalent to [44].

$$\mathbf{k}^{(t+1)} = \mathcal{DC}_\eta(\mathbf{k}^{(t)}, \mathbf{k}^{(0)}) = \mathbf{k}^{(t)} - \eta \mathcal{M}(\mathbf{k}^{(t)} - \mathbf{k}^{(0)}) \quad (9)$$

$\mathbf{x}^{(0)}$, derived by Eq. (2), serves as an initial estimate with aliasing artifacts. The iterative updates concluded with coil combination step as in Eq. (3), form the complete MRI reconstruction pipeline.

3.2 Unrolled Expended Model

UE enhances robustness by addressing a key but previously overlooked bottleneck: CSM estimation, which we identify as critical for robustness. When these maps are accurately estimated, they facilitate coherent combination of multi-coil data into a single high-SNR image and simplifies the subsequent denoising task, and boost final performance. When these maps are inaccurate, exacerbated under domain shift as shown in Fig. 3, these errors are amplified through subsequent network layers, cascading into complete reconstruction failure. Unlike

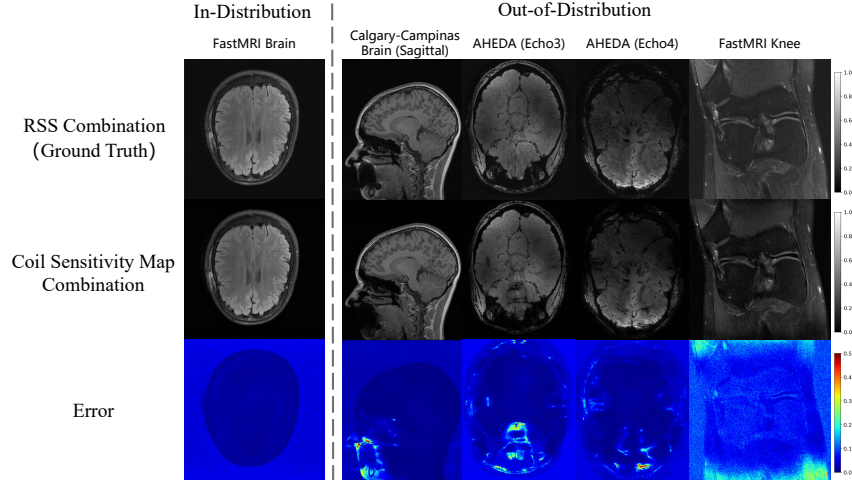


Fig. 3: Examples of CSM estimation

typical networks stabilized by normalization layers [4], unrolled models interleave denoisers with coil reduction/expansion steps, where these maps errors are amplified rather than corrected.

Examining Eq. (5), we observe that CSM can be circumvented entirely by reformulating the reconstruction target as individual coil images. This simple shift eliminates the risk of error propagation. The iterative step of UE is below

$$\tilde{\mathbf{x}}^{(t)} = \mathbf{x}^{(t)} + \mathcal{D}_\theta^{(t)}(\mathbf{x}^{(t)}) \quad (10)$$

$$\mathbf{k}^{(t)} = \mathcal{F}(\tilde{\mathbf{x}}^{(t)}) \quad (11)$$

$$\mathbf{k}^{(t+1)} = \mathcal{DC}_\eta(\mathbf{k}^{(t)}, \mathbf{k}^{(0)}) \quad (12)$$

$$\mathbf{x}^{(t+1)} = \mathcal{F}^{-1}(\mathbf{k}^{(t+1)}) \quad (13)$$

where $\mathcal{D}_\theta^{(t)}$ takes input of $\mathbf{x}^{(t)} \in \mathbb{C}^{N \times H \times W}$, differs from $\mathcal{R}(\mathbf{x}^{(t)}) \in \mathbb{C}^{H \times W}$ in Sec. 3.1. We treat multi coils as a batch dimension, allowing $\mathcal{D}_\theta^{(t)}$ unchanged for fair comparison with standard DUM. Exploiting inter-coil correlations within $\mathcal{D}_\theta^{(t)}$ is left for future research. This additional batch dimension increases computation, which is alleviated by the features introduced below.

3.3 Progressive Resolution

Unrolled Expanded model with Progressive resolution (UEP) is designed for efficient computation of high-resolution image by delaying high-resolution processing to later stages, minimizing computation in early cascades. Our core innovation is performing up-sampling via k-space expansion, where additional measurements populate the extended frequency region, adding authentic high-frequency

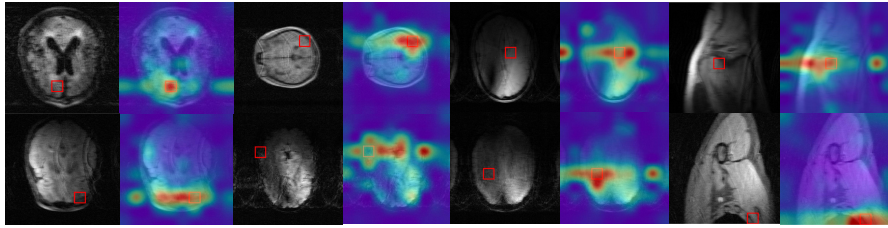


Fig. 4: Exmaples of attention scores

information, which cannot be achieved by image-space up-sampling operations. This novel up-sampling operation integrates naturally into the unrolled pipeline, leading to the following formulation for each stage

$$\tilde{\mathbf{x}}^{(t)} = \mathbf{x}^{(t)} + \mathcal{D}_\theta^{(t)}(\mathbf{x}^{(t)}) \quad (14)$$

$$\mathbf{k}^{(t)} = \mathcal{F}(\tilde{\mathbf{x}}^{(t)}) \quad (15)$$

$$\tilde{\mathbf{k}}^{(t)} = \mathcal{DC}_\eta(\mathbf{k}^{(t)}, \mathbf{k}^{(0)}) \quad (16)$$

$$\mathbf{k}^{(t+1)} = \mathcal{P}(\tilde{\mathbf{k}}^{(t)}, \mathbf{k}^{(0)}) \quad (17)$$

$$\mathbf{x}^{(t+1)} = \mathcal{F}^{-1}(\mathbf{k}^{(t+1)}) \quad (18)$$

where $\mathbf{x}^{(t)}, \tilde{\mathbf{x}}^{(t)}, \mathbf{k}^{(t)}, \tilde{\mathbf{k}}^{(t)} \in \mathbb{C}^{N \times h^{(t)} \times w^{(t)}}$, $h^{(t)}, w^{(t)}$ define the progressive resolution schedule for t -th stage. \mathcal{P} is the k-space padding operator, filling expanded region with acquired measurements where available, and zero elsewhere. Unlike UE and standard DUM, the initial estimate $\mathbf{x}^{(0)}$ is derived by Eq. (2) after cropping $\mathbf{k}^{(0)}$ to the central region with size of $h^{(0)} \times w^{(0)}$.

Almost all existing DUM approaches fall within a two-loops paradigm, an outer cascaded refinement loop with constant resolution, and an inner multi-resolution loop with U-shaped backbone. UEP is, to the best of our knowledge, the first design to unify cascaded refinement and resolution scheduling into a single, up-sampling-only loop, which substantially improves efficiency by operating at lower resolutions for the bulk of the computation.

Typical MRI sampling masks are denser in the center, leading to a higher sampling density of the initial cascades of UEP with smaller k-space support, translating to a lower effective acceleration factor, making the early reconstruction considerably easier. Thus, our progressive resolution design does more than just fit within the DUM framework, it inherently strengthens the progressive refinement nature of DUM.

3.4 Sparse Attention

Despite substantial acceleration from progressive resolution, the full-resolution final cascade is still computationally heavy for high-resolution images, when employing a standard ViT as \mathcal{D}_θ , whose full self-attention incurs quadratic complexity. Sparse attention is introduced by designing a sparsity pattern that determines which spatial locations attend to each other, computing attention only

where it is meaningful and omitting it elsewhere to overcome the quadratic complexity. Together with UEP, this forms our final model, UEPS.

We propose a novel sparsity pattern tailored for MRI, exploiting the fact that MRI undersampling, and thus aliasing, is anisotropic, a critical distinction from natural image tasks that assume isotropic spatial correlations. Acceleration in MRI is accomplished by undersampling along the phase-encode axis, while the readout direction is always fully sampled as undersampling it does not shorten scan time. From Fourier principles, multiplying k-space by a separable 1D mask corresponds to convolving the image with a 1D kernel, producing aliasing exclusively along that dimension. Following the convention in [58], we denote a 1D mask along the k_x axis, and the accordingly aliasing along the x axis.

Since the primary goal of \mathcal{D}_θ is to remove x-axis aliasing, meaningful attention is expected to occur predominantly along x. As shown in Fig. 4, attention maps from UE with standard ViT confirm this assumption, with scores concentrated along the x-axis. Rather than learning the sparsity pattern from data with standard ViT, we design it explicitly to maximize efficiency. Concretely, we define that each pixel attends to all other pixels within the same row and its n adjacent rows, as shown in Fig. 2. Additionally, we interleave sparse self-attention layers with full attention layers to preserve global context, following SOTA sparse attention designs in large language models [1, 33, 47].

By faithfully leveraging MRI physical principles, namely k-space acquisition and 1D undersampling, UEPS achieves simultaneous gains in efficiency and performance, circumventing the typical trade-off between the two.

4 Experiments and Results

4.1 Experimental Setups

For rigorous robustness assessment, we construct a large and diverse zero-shot transfer benchmark comprising 10 out-of-distribution (OOD) test sets drawn from 5 publicly available resources, all of which contain fully-sampled multi-coil raw cartesian k-space data, as shown in Tab. 1. All methods are trained solely on the FastMRI Brain training set [58], the largest public dataset, designating its test split as in-distribution (ID) and all other datasets as OOD test sets for zero-shot transfer evaluation. Our benchmark encompasses a wide range of clinical distribution shifts across anatomy, view, sequence type, contrast, scanner vendor, field strength, and coil configuration, reflecting real-world variability. As resolution varies across datasets, we resample all k-space data to 320×320 matrix size [58] via corresponding image-space cropping or padding to ensure compatibility with all methods, following [14, 50]. Since the number of coils varies across data, we only include methods capable of handling arbitrary coil configurations in our comparison.

To ensure comprehensive comparison, we compare against representative leading methods from each major category: DUM [20, 44, 50], end-to-end networks [28, 38], diffusion models [6], and untrained methods [22, 42], representing

Table 1: Summary of MRI Datasets. 3D dataset is treated as multi-slice 2D data with certain anatomical view, including CC-359 converted to axial and sagittal views as two separate test sets, and AHEAD converted to axial view. AHEAD sequence contains 5 echoes, each forming a separate test set.

Split	Dataset Name	Part	View	Sequence	Vendor	B0	Coils	Subj.	Slices
Train	FastMRI Brain[58]	brain	axial	2D FSE	Siemens	3T/1.5T	2-28	4469	70748
Test(ID)	FastMRI Brain[58]	brain	axial	2D FSE	Siemens	3T/1.5T	2-24	558	8852
Test (OOD)	FastMRI Knee[58]	knee	coronal	2D FSE	Siemens	3T/1.5T	15	150	5427
	Stanford 2D [5]	mix	mix	2D FSE	GE	3T	3-32	89	2037
	CC-359(Axi) [43]	brain	axial	3D MP-RAGE	GE	3T	12	67	13802
	CC-359(Sag) [43]	brain	sagittal	3D MP-RAGE	GE	3T	12	67	9490
	M4Raw(GRE) [34]	brain	axial	2D GRE	Xingaoyi	0.3T	4	183	6588
	AHEAD(Echo1)[3]	brain	axial	3D MP2RAGEME	Philips	7T	32	20	3240
	AHEAD(Echo2)[3]	brain	axial	3D MP2RAGEME	Philips	7T	32	20	3240
	AHEAD(Echo3)[3]	brain	axial	3D MP2RAGEME	Philips	7T	32	20	3240
	AHEAD(Echo4)[3]	brain	axial	3D MP2RAGEME	Philips	7T	32	20	3240
	AHEAD(Echo5)[3]	brain	axial	3D MP2RAGEME	Philips	7T	32	20	3240

the full spectrum of current MRI reconstruction techniques. To ensure fair comparison, DUM and end-to-end models are retrained under our settings [20, 28, 38, 44, 50]; diffusion models use provided model weights [6]; untrained methods are directly applied in a zero-shot manner [22, 42].

For all methods, undersampled k-space data is generated retrospectively using equispaced mask with $4\times$ acceleration and 8% fully sampled center, the dominant setting in MRI reconstruction literature [58]. Reconstruction quality is assessed via PSNR and SSIM, both take the maximum value of the 3D volume for normalization, and the ground truth is obtained from fully sampled data combined via RSS. All runtime measurements are performed on one 5090 GPU, unless otherwise specified. Due to suboptimal results from our initial DDS implementation, we re-evaluated it using Gaussian sampling masks and MVUE target for metrics, strictly adhering to the original setting [6].

4.2 Implementation Details

Our full attention ViT baseline is built on [35], integrating additional architectural advances, such as 2D rotary position embedding [15, 46], SwiGLU as the feedforward network [40]. Sparse attention ViT is implemented within the framework of flex attention [10]. We set the entire UEPS model to approximately 120M parameters with patch size of 8, unless otherwise specified.

4.3 Zero-shot Transfer Benchmark Results

Figure 1, together with the qualitative comparison in Fig. 5, provides clear evidence that UEPS markedly improves robustness, consistently surpassing existing SOTA methods across all out-of-distribution test sets and achieving a large performance margin in aggregate. The strong in-distribution performance of other DUM methods and end-to-end methods fails to generalize to OOD settings,

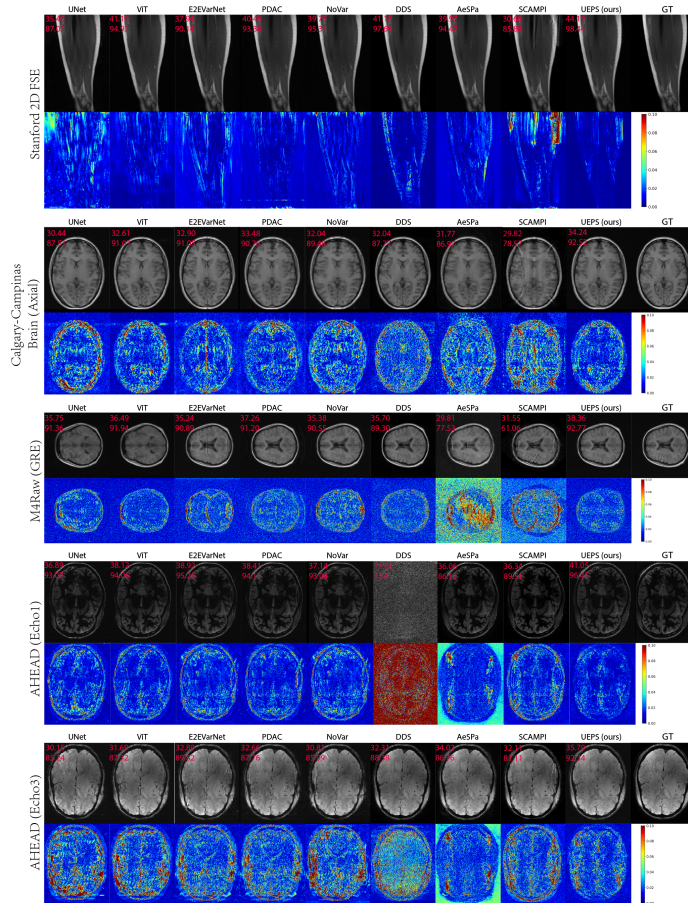


Fig. 5: Reconstruction examples from the zero-shot transfer benchmark, each with PSNR/SSIM shown on the top left corner.

further underscoring the need of zero-shot transfer evaluation for real-world deployment. Untrained methods trade off in-distribution performance as expected, however, this sacrifice brings no OOD advantage over supervised techniques. Remarkably, UEPS delivers robust performance with low latency, enabled by two efficiency-driven features that make real-time deployment feasible.

4.4 Ablation Studies

We perform ablation experiments to evaluate the individual impact of our three features on robustness and efficiency. As shown in Tab. 2, UE provides the dominant robustness improvement, as expected, followed by the transition to a ViT backbone, with progressive resolution and sparse attention yielding additional but smaller gains. Although UE increases runtime, the subsequent adoption of a ViT backbone, progressive resolution, and sparse attention each contribute

Table 2: Ablation study results on three selected OOD test sets and the average of all ten OOD test sets. Runtime varies across test sets due to different coil counts: M4Raw(GRE) of 4, FastMRI Knee of 15, AHEAD(Echo3) of 32. Best in bold.

Dataset	Metric	Model				
		E2EVarNet _[44]	UE-UNet	UE-ViT	UEP-ViT	UEPS _(Ours)
M4Raw GRE	PSNR(dB)↑	36.72±1.98	37.38±1.88	37.80 ±1.68	37.62±1.81	37.47±1.77
	SSIM(%)↑	91.33±1.68	91.78±1.57	91.93±1.46	92.05 ±1.50	91.94±1.51
	Runtime(ms)↓	7.81±0.23	19.98±0.28	16.51±0.01	7.31±0.22	6.50 ±0.03
FastMRI Knee	PSNR(dB)↑	39.23±4.32	39.68±3.80	39.91±3.83	39.97±3.91	40.07 ±3.93
	SSIM(%)↑	91.56±6.40	92.11±5.95	92.08±6.25	92.31±6.07	92.38 ±6.08
	Runtime(ms)↓	17.55 ±0.31	63.96±0.45	60.78±0.55	26.29±0.12	23.61±0.39
AHEAD Echo3	PSNR(dB)↑	35.07±2.54	37.09±2.68	37.34±2.50	37.57±2.55	37.86 ±2.54
	SSIM(%)↑	90.18±4.05	92.80±2.90	93.11±2.63	93.41±2.60	93.66 ±2.52
	Runtime(ms)↓	27.60 ±0.46	225.89±0.30	132.56±0.09	57.93±0.48	51.85±0.11
Average	PSNR(dB)↑	36.78	37.54	37.90	37.98	38.13
	SSIM(%)↑	91.88	92.82	93.08	93.25	93.39
	Runtime(ms)↓	21.77	152.51	97.28	42.32	38.02

to computational savings, cumulatively reducing runtime to a level comparable with the E2EVarNet baseline. Note the E2EVarNet results in Tab. 2 are from our reimplementaion of [44], which yields a stronger baseline than the original.

Figure 6 illustrates the distinct efficiency roles: progressive resolution reduces computation across all patch counts, while sparse attention specifically addresses the quadratic bottleneck at high patch counts, where full self-attention becomes prohibitively expensive.

4.5 Multi-Resolution Comparison

We evaluate our progressive resolution design against competitive multi-resolution architectures from both the general vision domain and prior MRI reconstruction

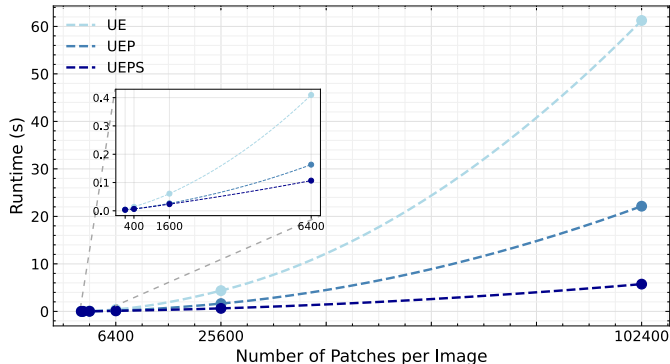


Fig. 6: Runtime Comparison

Table 3: Comparison of multi-resolution methods. Best in bold.

Dataset	Metric	Model				
		GrappaNet _[45]	Restormer _[57]	ASTv2 _[60]	PDAC _[50]	UEPS _(Ours)
M4Raw GRE	PSNR(dB)↑	36.40±2.09	36.50±2.09	36.93±1.96	36.63±1.93	37.32 ±1.80
	SSIM(%)↑	91.01±1.77	91.30±1.75	91.59±1.65	90.31±1.93	91.76 ±1.54
	Runtime(ms)↓	4.96±0.28	107.34±0.06	87.21±0.06	98.99±0.89	2.32 ±0.29
FastMRI Knee	PSNR(dB)↑	38.88±3.85	39.83±3.74	39.90 ±3.75	38.30±3.92	39.87±3.72
	SSIM(%)↑	91.54±5.84	92.38±5.76	92.40 ±5.78	90.38±6.59	92.08±6.06
	Runtime(ms)↓	15.68±0.63	194.67±0.55	185.55±0.32	113.22±7.42	7.43 ±0.04
AHEAD Echo3	PSNR(dB)↑	35.34±2.43	35.82±2.69	35.38±2.73	33.86±2.68	37.24 ±2.57
	SSIM(%)↑	91.41±3.14	91.94±3.20	91.45±3.52	87.85±4.62	93.01 ±2.74
	Runtime(ms)↓	39.44±0.71	755.35±0.41	607.07±0.46	122.62±2.44	16.14 ±0.78
Average	PSNR(dB)↑	36.03	36.71	36.72	35.94	37.57
	SSIM(%)↑	91.59	92.24	92.10	90.28	92.76
	Runtime(ms)↓	28.66	543.00	439.88	114.94	11.85

studies. we select Restormer [57], a cornerstone in image restoration with U-shaped transformer, along with a latest improved variant [60]. Given the high memory footprint of these two models, we use a reduced configuration with approximately 30M parameters and a single UE cascade, the maximum feasible within our GPU memory. Two prior multi-resolution MRI methods are included, GrappaNet [45], a UNet-based coil-wise approach similar to our UE, and PDAC [50], a DUM approach with inner-cascade multi-resolution. GrappaNet and our model are likewise configured with 30M parameters for fair comparison, while PDAC uses its original configuration with roughly 130M parameters.

Table 3 shows our model achieves top robustness, followed by Restormer and ASTv2, while PDAC lags due to its fragile CSM estimation. The strong representational capacity of Restormer and ASTv2 comes at the cost of substantial computational burden and GPU memory consumption. In contrast, UEPS employs a novel architecture that merges cascaded refinement with progressive resolution scheduling in a single, up-sampling-only loop, thus concentrating most computation at low resolutions for superior efficiency. Note that UEPS performance in Tab. 3 is worse than that in Tab. 2 due to reduced model size.

4.6 Sparse Attention Comparison

We compare the proposed sparse attention design with representative sparse attention approaches in vision tasks. For methods with static sparsity pattern, we select Swin [32], CSWin [11], and NAT [18], with the corresponding sparsity patterns shown in Fig. 2. We also include one dynamic sparse attention method, Sparge [59]. All compared models share the same UEP framework, with only the transformer backbone varied to ensure fair comparison. Note that the runtime of Sparge is measured on a 4090 GPU and appropriately converted to

Table 4: Comparison of sparse attention methods. Best in bold.

Dataset	Metric	Model				
		Swin _[32]	CSWin _[11]	NAT _[18]	SpargE _[59]	UEPS _(Ours)
M4Raw GRE	PSNR(dB)↑	37.18±1.82	37.47±1.68	37.59 ±1.80	36.58±1.86	37.47±1.77
	SSIM(%)↑	91.61±1.56	91.95 ±1.46	91.92±1.53	91.09±1.68	91.94±1.51
	Runtime(ms)↓	6.91±0.38	6.58±0.52	6.77±0.39	8.60±0.48	6.50 ±0.03
FastMRI Knee	PSNR(dB)↑	39.94±3.80	39.90±3.96	39.98±3.82	39.71±3.81	40.07 ±3.93
	SSIM(%)↑	92.29±5.97	92.20±6.21	92.35±5.96	92.10±6.03	92.38 ±6.08
	Runtime(ms)↓	24.60±0.66	23.54 ±0.95	24.14±0.24	29.79±0.18	23.61±0.39
AHEAD Echo3	PSNR(dB)↑	37.05±2.62	37.60±2.60	37.25±2.57	36.98±2.63	37.86 ±2.54
	SSIM(%)↑	92.94±2.73	93.43±2.61	93.00±2.69	92.69±2.83	93.66 ±2.52
	Runtime(ms)↓	53.93±0.15	51.15 ±0.54	53.25±0.53	64.72±0.05	51.85±0.11
Average	PSNR(dB)↑	37.62	38.01	37.80	37.36	38.13
	SSIM(%)↑	92.92	93.28	93.07	92.56	93.39
	Runtime(ms)↓	39.72	37.41	38.96	47.57	38.02

5090-equivalent for fair comparison, as it could not be run on our 5090 hardware. Thanks to the robust UEP foundation, all tested sparse attention patterns achieve similarly high performance, as shown in Tab. 4. Our MRI-tailored sparse attention marginally outperforms general vision counterparts by explicitly leveraging MRI’s 1D aliasing nature.

5 Limitations

A limitation is our exclusive focus on model design for robustness; diverse training data, proven to boost robustness in MRI [29, 30] and vision tasks [24, 36], remains unexplored. This orthogonal direction offers a clear avenue for future integration. While robust to variations in anatomy, view, contrast, and scanner vendor, our method, like other DUMs, may generalize poorly to unseen masks and acceleration factors. Prior work indicates this could be alleviated through training with diverse sampling patterns [29]. This work addresses 2D reconstruction, though MRI is intrinsically 3D (isotropic 3D acquisition or multi-slice 2D acquisition). Previous studies demonstrate improved performance with 3D input [54], motivating future extension of sparse attention with extra dimension.

6 Conclusion

We significantly improve MRI reconstruction robustness through three MRI-grounded design features: unrolled expended model, progressive resolution, and sparse attention. These innovations yield simultaneous gains in performance and speed. A large-scale zero-shot transfer benchmark across 10 diverse OOD datasets confirms that UEPS consistently and substantially outperforms existing methods, establishing a new standard for robust real-world MRI reconstruction.

References

1. Agarwal, S., Ahmad, L., Ai, J., Altman, S., Applebaum, A., Arbus, E., Arora, R.K., Bai, Y., Baker, B., Bao, H., et al.: gpt-oss-120b & gpt-oss-20b model card. arXiv preprint arXiv:2508.10925 (2025)
2. Aggarwal, H.K., Mani, M.P., Jacob, M.: Modl: Model-based deep learning architecture for inverse problems. *IEEE transactions on medical imaging* **38**(2), 394–405 (2018)
3. Alkemade, A., Mulder, M.J., Groot, J.M., Isaacs, B.R., van Berendonk, N., Lute, N., Isherwood, S.J., Bazin, P.L., Forstmann, B.U.: The amsterdam ultra-high field adult lifespan database (ahead): A freely available multimodal 7 tesla submillimeter magnetic resonance imaging database. *NeuroImage* **221**, 117200 (2020)
4. Ba, J.L., Kiros, J.R., Hinton, G.E.: Layer normalization. arXiv preprint arXiv:1607.06450 (2016)
5. Cheng, J.: Stanford 2d fse dataset. mridata.org (2018), <http://mridata.org/list?project=Stanford%202D%20FSE>
6. Chung, H., Lee, S., Ye, J.C.: Decomposed diffusion sampler for accelerating large-scale inverse problems. arXiv preprint arXiv:2303.05754 (2023)
7. Darestani, M.Z., Chaudhari, A.S., Heckel, R.: Measuring robustness in deep learning based compressive sensing. In: *International Conference on Machine Learning*. pp. 2433–2444. PMLR (2021)
8. Darestani, M.Z., Heckel, R.: Accelerated mri with un-trained neural networks. *IEEE Transactions on Computational Imaging* **7**, 724–733 (2021)
9. Darestani, M.Z., Nath, V., Li, W., He, Y., Roth, H.R., Xu, Z., Xu, D., Heckel, R., Zhao, C.: Ir-freestormer: Iterative refinement with fourier-based restormer for accelerated mri reconstruction. In: *Proceedings of the IEEE/CVF winter conference on applications of computer vision*. pp. 7655–7664 (2024)
10. Dong, J., Feng, B., Guessous, D., Liang, Y., He, H.: Flex attention: A programming model for generating optimized attention kernels. arXiv preprint arXiv:2412.05496 **2**(3), 4 (2024)
11. Dong, X., Bao, J., Chen, D., Zhang, W., Yu, N., Yuan, L., Chen, D., Guo, B.: Cswin transformer: A general vision transformer backbone with cross-shaped windows. In: *Proceedings of the IEEE/CVF conference on computer vision and pattern recognition*. pp. 12124–12134 (2022)
12. Dosovitskiy, A., Beyer, L., Kolesnikov, A., Weissenborn, D., Zhai, X., Unterthiner, T., Dehghani, M., Minderer, M., Heigold, G., Gelly, S., et al.: An image is worth 16x16 words: Transformers for image recognition at scale. arXiv preprint arXiv:2010.11929 (2020)
13. Dumoulin, V., Visin, F.: A guide to convolution arithmetic for deep learning. arXiv preprint arXiv:1603.07285 (2016)
14. Fabian, Z., Tinaz, B., Soltanolkotabi, M.: Humus-net: Hybrid unrolled multi-scale network architecture for accelerated mri reconstruction. *Advances in Neural Information Processing Systems* **35**, 25306–25319 (2022)
15. Fang, Y., Sun, Q., Wang, X., Huang, T., Wang, X., Cao, Y.: Eva-02: A visual representation for neon genesis. *Image and Vision Computing* **149**, 105171 (2024)
16. Feng, R., Wu, Q., Feng, J., She, H., Liu, C., Zhang, Y., Wei, H.: Imjense: scan-specific implicit representation for joint coil sensitivity and image estimation in parallel mri. *IEEE Transactions on Medical Imaging* **43**(4), 1539–1553 (2023)
17. Hammernik, K., Klatzer, T., Kobler, E., Recht, M.P., Sodickson, D.K., Pock, T., Knoll, F.: Learning a variational network for reconstruction of accelerated mri data. *Magnetic resonance in medicine* **79**(6), 3055–3071 (2018)

18. Hassani, A., Walton, S., Li, J., Li, S., Shi, H.: Neighborhood attention transformer. In: Proceedings of the IEEE/CVF conference on computer vision and pattern recognition. pp. 6185–6194 (2023)
19. He, X., Quan, Y., Xu, R., Ji, H.: A universal scale-adaptive deformable transformer for image restoration across diverse artifacts. In: Proceedings of the IEEE/CVF Conference on Computer Vision and Pattern Recognition. pp. 12731–12741 (2025)
20. Jatyani, A.S., Wang, J., Chandrashekar, A., Wu, Z., Liu-Schiaffini, M., Tolooshams, B., Anandkumar, A.: A unified model for compressed sensing mri across undersampling patterns. In: Proceedings of the Computer Vision and Pattern Recognition Conference. pp. 26004–26013 (2025)
21. Johnson, P.M., Jeong, G., Hammernik, K., Schlemper, J., Qin, C., Duan, J., Rueckert, D., Lee, J., Pezzotti, N., De Weerd, E., et al.: Evaluation of the robustness of learned mr image reconstruction to systematic deviations between training and test data for the models from the fastmri challenge. In: International Workshop on Machine Learning for Medical Image Reconstruction. pp. 25–34. Springer (2021)
22. Joo, J., Kim, H., Won, H., Lee, D., Eo, T., Hwang, D.: Aespa: Attention-guided self-supervised parallel imaging for mri reconstruction. In: Proceedings of the Computer Vision and Pattern Recognition Conference. pp. 5217–5226 (2025)
23. Jun, Y., Shin, H., Eo, T., Hwang, D.: Joint deep model-based mr image and coil sensitivity reconstruction network (joint-icnet) for fast mri. In: Proceedings of the IEEE/CVF conference on computer vision and pattern recognition. pp. 5270–5279 (2021)
24. Kirillov, A., Mintun, E., Ravi, N., Mao, H., Rolland, C., Gustafson, L., Xiao, T., Whitehead, S., Berg, A.C., Lo, W.Y., et al.: Segment anything. In: Proceedings of the IEEE/CVF international conference on computer vision. pp. 4015–4026 (2023)
25. Knoll, F., Hammernik, K., Kobler, E., Pock, T., Recht, M.P., Sodickson, D.K.: Assessment of the generalization of learned image reconstruction and the potential for transfer learning. *Magnetic resonance in medicine* **81**(1), 116–128 (2019)
26. Leynes, A.P., Deveshwar, N., Nagarajan, S.S., Larson, P.E.: Scan-specific self-supervised bayesian deep non-linear inversion for undersampled mri reconstruction. *IEEE transactions on medical imaging* **43**(6), 2358–2369 (2024)
27. Liang, J., Cao, J., Sun, G., Zhang, K., Van Gool, L., Timofte, R.: Swinir: Image restoration using swin transformer. In: Proceedings of the IEEE/CVF international conference on computer vision. pp. 1833–1844 (2021)
28. Lin, K., Heckel, R.: Vision transformers enable fast and robust accelerated mri. In: International Conference on medical imaging with deep learning. pp. 774–795. PMLR (2022)
29. Lin, K., Heckel, R.: Robustness of deep learning for accelerated mri: benefits of diverse training data. *arXiv preprint arXiv:2312.10271* (2023)
30. Lin, K., Krainovic, A., Wang, K., Heckel, R.: Improving deep learning for accelerated mri with data filtering. *arXiv preprint arXiv:2508.13822* (2025)
31. Liu, Y., Pang, Y., Li, J., Chen, Y., Yap, P.T.: Architecture-agnostic untrained network priors for image reconstruction with frequency regularization. In: European Conference on Computer Vision. pp. 341–358. Springer (2024)
32. Liu, Z., Lin, Y., Cao, Y., Hu, H., Wei, Y., Zhang, Z., Lin, S., Guo, B.: Swin transformer: Hierarchical vision transformer using shifted windows. In: Proceedings of the IEEE/CVF international conference on computer vision. pp. 10012–10022 (2021)
33. Lu, E., Jiang, Z., Liu, J., Du, Y., Jiang, T., Hong, C., Liu, S., He, W., Yuan, E., Wang, Y., et al.: Moba: Mixture of block attention for long-context llms. *arXiv preprint arXiv:2502.13189* (2025)

34. Lyu, M., Mei, L., Huang, S., Liu, S., Li, Y., Yang, K., Liu, Y., Dong, Y., Dong, L., Wu, E.X.: M4raw: A multi-contrast, multi-repetition, multi-channel mri k-space dataset for low-field mri research. *Scientific Data* **10**(1), 264 (2023)
35. Peebles, W., Xie, S.: Scalable diffusion models with transformers. In: *Proceedings of the IEEE/CVF international conference on computer vision*. pp. 4195–4205 (2023)
36. Radford, A., Kim, J.W., Hallacy, C., Ramesh, A., Goh, G., Agarwal, S., Sastry, G., Askell, A., Mishkin, P., Clark, J., et al.: Learning transferable visual models from natural language supervision. In: *International conference on machine learning*. pp. 8748–8763. PmLR (2021)
37. Rao, Y., Zhao, W., Liu, B., Lu, J., Zhou, J., Hsieh, C.J.: Dynamicvit: Efficient vision transformers with dynamic token sparsification. *Advances in neural information processing systems* **34**, 13937–13949 (2021)
38. Ronneberger, O., Fischer, P., Brox, T.: U-net: Convolutional networks for biomedical image segmentation. In: *International Conference on Medical image computing and computer-assisted intervention*. pp. 234–241. Springer (2015)
39. Schlemper, J., Caballero, J., Hajnal, J.V., Price, A.N., Rueckert, D.: A deep cascade of convolutional neural networks for dynamic mr image reconstruction. *IEEE transactions on Medical Imaging* **37**(2), 491–503 (2017)
40. Shazeer, N.: Glu variants improve transformer. *arXiv preprint arXiv:2002.05202* (2020)
41. Shi, W., Caballero, J., Huszár, F., Totz, J., Aitken, A.P., Bishop, R., Rueckert, D., Wang, Z.: Real-time single image and video super-resolution using an efficient sub-pixel convolutional neural network. In: *Proceedings of the IEEE conference on computer vision and pattern recognition*. pp. 1874–1883 (2016)
42. Siedler, T.M., Jakob, P.M., Herold, V.: Enhancing quality and speed in database-free neural network reconstructions of undersampled mri with scampi. *Magnetic Resonance in Medicine* **92**(3), 1232–1247 (2024)
43. Souza, R., Lucena, O., Garrafa, J., Gobbi, D., Saluzzi, M., Appenzeller, S., Ritter, L., Frayne, R., Lotufo, R.: An open, multi-vendor, multi-field-strength brain mr dataset and analysis of publicly available skull stripping methods agreement. *NeuroImage* **170**, 482–494 (2018)
44. Sriram, A., Zbontar, J., Murrell, T., Defazio, A., Zitnick, C.L., Yakubova, N., Knoll, F., Johnson, P.: End-to-end variational networks for accelerated mri reconstruction. In: *International conference on medical image computing and computer-assisted intervention*. pp. 64–73. Springer (2020)
45. Sriram, A., Zbontar, J., Murrell, T., Zitnick, C.L., Defazio, A., Sodickson, D.K.: Grappanet: Combining parallel imaging with deep learning for multi-coil mri reconstruction. In: *Proceedings of the IEEE/CVF Conference on Computer Vision and Pattern Recognition*. pp. 14315–14322 (2020)
46. Su, J., Ahmed, M., Lu, Y., Pan, S., Bo, W., Liu, Y.: Roformer: Enhanced transformer with rotary position embedding. *Neurocomputing* **568**, 127063 (2024)
47. Team, G., Riviere, M., Pathak, S., Sessa, P.G., Hardin, C., Bhupatiraju, S., Hussenot, L., Mesnard, T., Shahriari, B., Ramé, A., et al.: Gemma 2: Improving open language models at a practical size. *arXiv preprint arXiv:2408.00118* (2024)
48. Uecker, M., Lai, P., Murphy, M.J., Virtue, P., Elad, M., Pauly, J.M., Vasanawala, S.S., Lustig, M.: Espirit—an eigenvalue approach to autocalibrating parallel mri: where sense meets grappa. *Magnetic resonance in medicine* **71**(3), 990–1001 (2014)
49. Uecker, M., Ong, F., Tamir, J.I., Bahri, D., Virtue, P., Cheng, J.Y., Zhang, T., Lustig, M.: Berkeley advanced reconstruction toolbox. In: *Proc. Intl. Soc. Mag. Reson. Med.* vol. 23, p. 9 (2015)

50. Wang, C., Guo, L., Wang, Y., Cheng, H., Yu, Y., Wen, B.: Progressive divide-and-conquer via subsampling decomposition for accelerated mri. In: Proceedings of the IEEE/CVF Conference on Computer Vision and Pattern Recognition. pp. 25128–25137 (2024)
51. Wang, H., Zhu, Y., Green, B., Adam, H., Yuille, A., Chen, L.C.: Axial-deeplab: Stand-alone axial-attention for panoptic segmentation. In: European conference on computer vision. pp. 108–126. Springer (2020)
52. Wang, P., Guo, P., Chai, K., Zhou, J., Xu, D., Jiang, S.: Sdum: A scalable deep unrolled model for universal mri reconstruction. arXiv preprint arXiv:2512.17137 (2025)
53. Wang, Z., Cun, X., Bao, J., Zhou, W., Liu, J., Li, H.: Uformer: A general u-shaped transformer for image restoration. In: Proceedings of the IEEE/CVF conference on computer vision and pattern recognition. pp. 17683–17693 (2022)
54. Xin, B., Ye, M., Axel, L., Metaxas, D.N.: Rethinking deep unrolled model for accelerated mri reconstruction. In: European Conference on Computer Vision. pp. 164–181. Springer (2024)
55. Yaman, B., Hosseini, S.A.H., Akçakaya, M.: Zero-shot self-supervised learning for mri reconstruction. arXiv preprint arXiv:2102.07737 (2021)
56. Yiasemis, G., Sonke, J.J., Sánchez, C., Teuwen, J.: Recurrent variational network: a deep learning inverse problem solver applied to the task of accelerated mri reconstruction. In: Proceedings of the IEEE/CVF conference on computer vision and pattern recognition. pp. 732–741 (2022)
57. Zamir, S.W., Arora, A., Khan, S., Hayat, M., Khan, F.S., Yang, M.H.: Restormer: Efficient transformer for high-resolution image restoration. In: Proceedings of the IEEE/CVF conference on computer vision and pattern recognition. pp. 5728–5739 (2022)
58. Zbontar, J., Knoll, F., Sriram, A., Murrell, T., Huang, Z., Muckley, M.J., Defazio, A., Stern, R., Johnson, P., Bruno, M., et al.: fastmri: An open dataset and benchmarks for accelerated mri. arXiv preprint arXiv:1811.08839 (2018)
59. Zhang, J., Xiang, C., Huang, H., Wei, J., Xi, H., Zhu, J., Chen, J.: Spargeattention: Accurate and training-free sparse attention accelerating any model inference. arXiv preprint arXiv:2502.18137 (2025)
60. Zhou, S., Pan, J., Yang, J.: Learning an adaptive sparse transformer for efficient image restoration. IEEE Transactions on Pattern Analysis and Machine Intelligence (2025)

UEPS: Robust and Efficient MRI Reconstruction

Supplementary Material

A Additional Experimental Setups

A.1 UEPS Architecture

The unrolled architecture of UEPS consists of 4 cascades with a progressive resolution schedule of 64×64 , 128×128 , 256×256 , and finally 320×320 . The ViT backbone within each cascade is configured identically with the following parameters: a patch size of 8, 10 transformer layers, an embedding width of 512, 8 attention heads, and an MLP intermediate size of 1280, which yields a total parameter count of approximately 120M. Flex attention based 1D sparse attention is applied for cascades where the number of patches per image is larger than 256, otherwise, standard scaled dot-product attention is used (*e.g.*, the initial 64×64 low-resolution cascade). We interleave sparse attention layers with full attention layers within the 10-layer transformer by setting the first and the last transformer layer as full attention, and the rest as sparse attention with $n = 1$ adjacent row on each side.

A.2 Training

Our model was trained end-to-end on the FastMRI Brain [58] training split with Mean Absolute Error (MAE) loss and the Adam optimizer for 30 epochs with a batch size of 8. The learning rate started with a linear warmup to the base value of 0.0003 over the first 1% of total iterations, and later decayed via a cosine annealing schedule down to 10% of the base value. To accelerate training, we utilized Automatic Mixed Precision (AMP) alongside PyTorch’s model compilation (`torch.compile`). To ensure fair evaluation, all models compared in our ablation and comparative experiments share the same training configuration, unless otherwise specified.

A.3 Ablation Studies

All models in the ablation studies have 4 unrolled cascades and approximately 120M parameters. The baseline E2EVarNet [44] employs a sensitivity map estimation UNet [38] (30 base channels, 4 pooling layers) and a denoiser UNet (60 base channels, 4 pooling layers) within each cascade. UE-Unet removes the sensitivity map estimation network and adjusts the UNet (64 base channels, 4 pooling layers). UE-ViT replaces UNet backbone with ViT backbone. For the computational efficiency analysis (Figure 6 of the main text), we measured the inference runtime of the UE, UEP, and UEPS models with an input resolution of 320×320 . Patch sizes vary across 32, 16, 8, 4, 2, and 1, which corresponds to the number of patches per image of 100, 400, 1600, 6400, 25600, and 102400, respectively.

A.4 Multi-Resolution Comparison

Training configuration was adjusted for all models in this study to accommodate the substantial memory and computational costs associated with Restormer [57] and ASTv2 [60]. Specifically, all models were trained for 20 epochs with 8-coil training data, randomly sampled from the original multi-coil data (which contains a variable number of coils). Restormer [57] and ASTv2 [60] have approximately 26M and 10M parameters, respectively, matching the configurations in their original publications.

A.5 Sparse Attention Comparison

To isolate the impact of the attention pattern itself, all models share the same parameter capacity of 120M. Furthermore, the sparsity patterns were configured to ensure that the effective receptive field (attention scope) for each patch is roughly comparable across models.

B Additional Zero-shot Transfer Benchmark Results

Figure 7 and Fig. 8 provide additional reconstruction examples from the in-distribution test set as well as all ten out-of-distribution test sets.

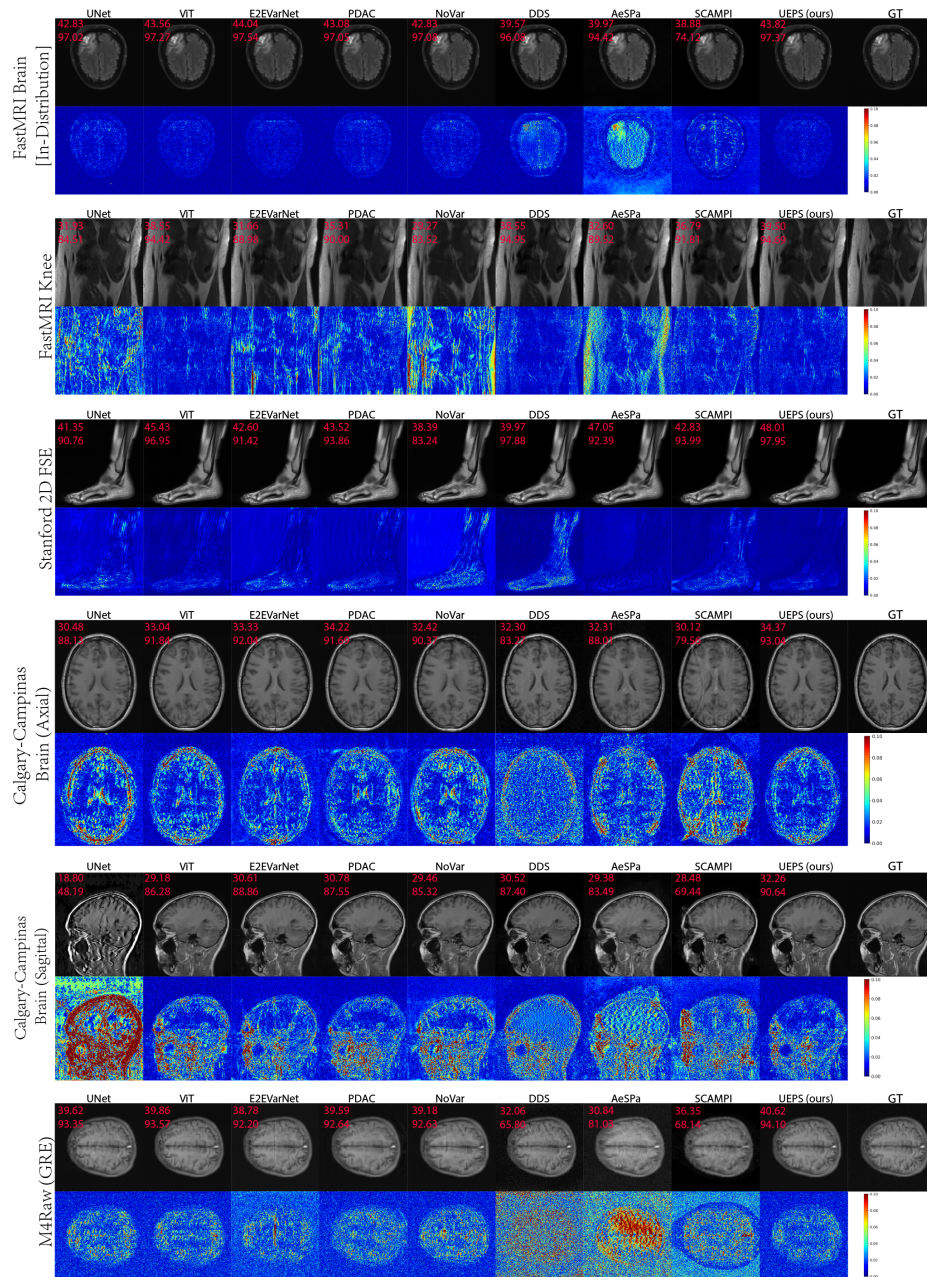


Fig. 7: Additional reconstruction examples, each with PSNR/SSIM shown on the top left corner (Part 1).

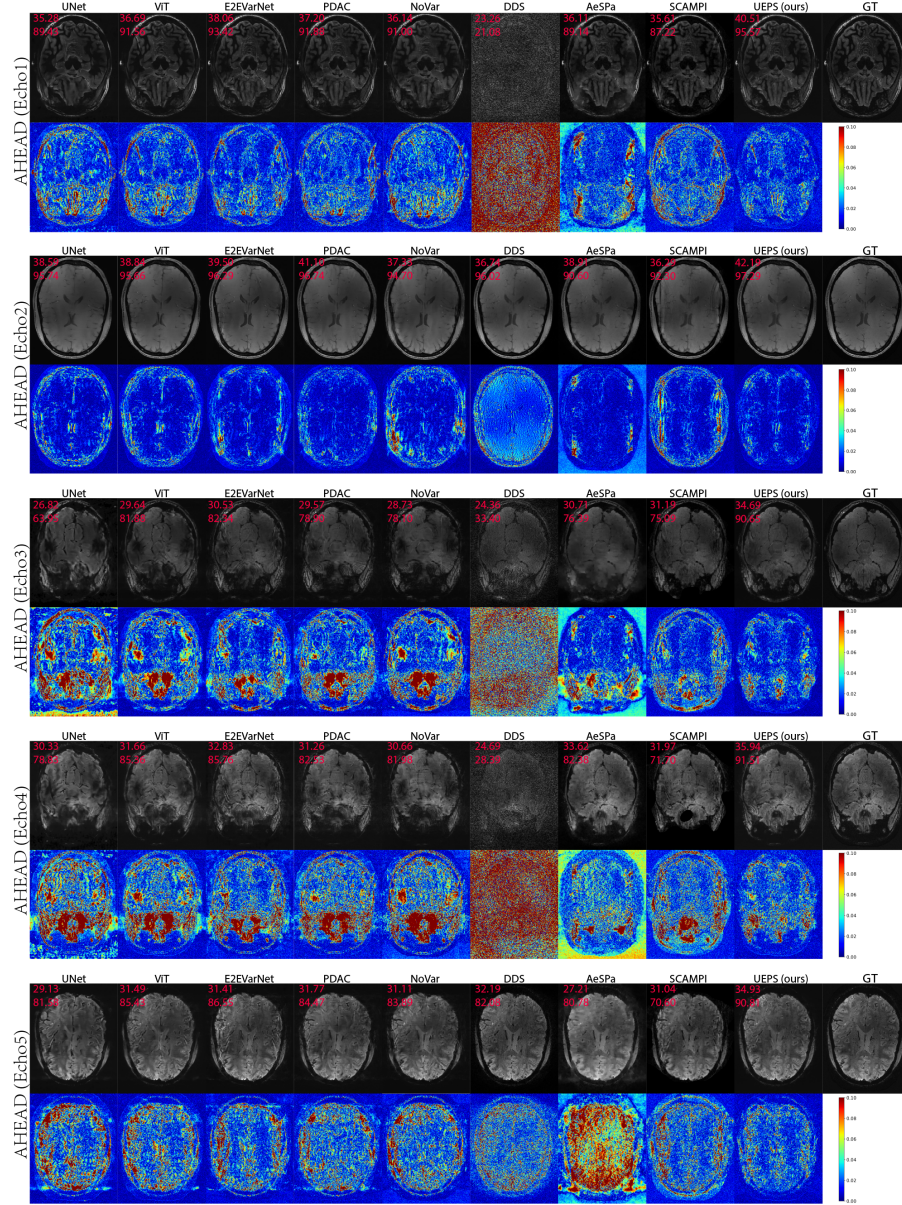


Fig. 8: Additional reconstruction examples, each with PSNR/SSIM shown on the top left corner (Part 2).